HHS Public Access

Author manuscript

J Nucl Med. Author manuscript; available in PMC 2018 February 07.

Published in final edited form as:

J Nucl Med. 2012 April ; 53(4): 546–551. doi:10.2967/jnumed.111.091421.

Introducing Parametric Fusion PET/MRI of Primary Prostate Cancer

Hyunjin Park[1,2], **David Wood**[3], **Hero Hussain**[1], **Charles R. Meyer**[1], **Rajal B. Shah**[4], **Timothy D. Johnson**[5], **Thomas Chenevert**[1], and **Morand Piert**[1]

[1]Department of Radiology, University of Michigan, Ann Arbor, Michigan

[2]Department of Biomedical Engineering, Gachon University, Incheon, South Korea

[3]Department of Urology, University of Michigan, Ann Arbor, Michigan

[4]Department of Pathology, University of Michigan, Ann Arbor, Michigan

[5]Department of Biostatistics, University of Michigan, Ann Arbor, Michigan

Abstract

We assessed the performance of parametric fusion PET/MRI based on ^{11}C-choline PET/CT and apparent diffusion coefficient (ADC) maps derived from diffusion-weighted MRI for the identification of primary prostate cancer.

Methods—^{11}C-choline PET/CT and MRI were performed in 17 patients with untreated primary prostate cancer, followed by prostatectomy. Registration of in vivo imaging with histology was achieved using a mutual-information objective function and by performing ex vivo MRI of the prostatectomy specimen (obtained at 3 T) and whole-mount sectioning with block-face photography as intermediate steps. Data analysis included volumetrically registered whole-mount histology with Gleason scoring, ^{11}C-choline, and ADC data (obtained at 1.5 T). Volumes of interest were defined on the basis of histologically proven tumor tissue to calculate tumor–to–benign prostate background ratios (TBRs) for ^{11}C-choline, ADC, and a derived fusion PET/MRI parameter calculating the quotient of ^{11}C-choline over ADC ($P_{CHOL/ADC}$).

Results—Fifty-one tumor nodules were identified at pathology. The TBRs for ^{11}C-choline ($P < 0.05$) and $P_{CHOL/ADC}$ ($P < 0.005$) were significantly higher in prostate cancers with a Gleason score of ≥3 + 4 than with a Gleason score of ≤3 + 3 disease and controls. For Gleason ≥ 3 + 4, the ADC TBRs were significantly lower than controls and Gleason ≤ 3 + 3 disease ($P < 0.05$). The absolute value of TBRs obtained from Gleason ≥ 3 + 4 cancers increased from ADC to ^{11}C-choline PET/CT and from ^{11}C-choline PET/CT to $P_{CHOL/ADC}$, with each step being statistically significant.

Conclusion—Our data indicate that parametric PET/MRI using $P_{CHOL/ADC}$ improves lesion-to-background contrast (TBRs) of Gleason ≥ 3 + 4 disease, compared with ^{11}C-choline PET/CT or diffusion-weighted MRI, and thus hold promise that parametric imaging performed on hybrid

For correspondence or reprints contact: Morand Piert, University of Michigan Health System, Department of Radiology, Division of Nuclear Medicine, University Hospital B1G505C, 1500 E. Medical Center Dr., Ann Arbor, MI 48109-0028. mpiert@umich.edu.

PET/MRI may further improve identification and localization of significant primary prostate cancer.

Keywords

PET/MRI; ^{11}C-choline; diffusion-weighted MRI; fusion imaging; prostate cancer

In the past 20 y, imaging of prostate cancer with CT, hybrid PET and CT (PET/CT), and MRI has rapidly developed for disease identification, staging, and management of treatment. Each modality has, however, well-known limitations inherent to anatomic and molecular imaging approaches that limit their diagnostic accuracy for the assessment of tumor stage and therapy response. For primary prostate cancer, several key clinical imaging scenarios exist: the identification of suspected prostate cancer (elevated prostate-specific antigen with previous negative biopsy), localization of clinically significant (more aggressive) primary disease, and detection of local and distant metastatic disease.

PET/CT with ^{11}C- and ^{18}F-choline has shown promise in the detection of prostate cancer, especially in the setting of recurrent and metastatic disease (1–4). Studies evaluating ^{11}C-choline for the detection of primary prostate cancer have provided mixed results (5–8), potentially because of overlap with benign prostate hyperplasia and prostatitis (9) and a considerable uncertainty about the true location of disease in relation to the imaging findings they were felt to represent. To overcome these technical limitations, we recently developed a registration method using a standard mutual-information objective function and thin-plate spline warping to register PET/CT and histology in prostate cancer (10). This registration technique—using high-resolution ex vivo MRI of the prostatectomy specimen and whole-mount histology— allowed the assessment of imaging findings associated with various histologic features, most importantly the local Gleason score. Using this technique in a patient population specifically selected to minimize potential inflammation from recent prostate biopsies or clinical signs of prostatitis, we identified that ^{11}C-choline preferentially localizes to aggressive primary prostate cancer when using tumor-to-normal background ratios, however, with considerable overlap to low-grade disease and benign tissues (11).

Anatomic MRI of primary prostate cancer has rapidly developed in the last decade. More recently, diffusion-weighted MRI (DWI) using apparent diffusion coefficient (ADC) maps has been applied. DWI techniques are based on the molecular mobility of water, which is sensitive to interaction with intracellular elements, macromolecules, cell membranes, cell density, and microstructural organization (12). DWI has identified restricted water diffusion in several malignancies, including prostate cancer (13,14). Recent studies performed in untreated primary prostate cancer suggested a subtle but significant negative correlation of ADCs with Gleason scores; thus, DWI ADC may be helpful in identifying peripheral zone cancers of intermediate and high risk (14–18).

To overcome specific limitations of morphologic and molecular imaging, hybrid PET/MRI scanners have most recently been introduced into clinical practice (19,20). Such systems promise optimal spatial and temporal coregistration of PET and MRI data, with the added benefit of performing functional MRI. It is still unknown whether such devices, compared with their established individual components performed separately, will indeed hold the

promise of improving clinical imaging (21). Here, we investigated for the first time whether the combination of ^{11}C-choline PET/CT and DWI may improve lesion detection of primary prostate cancer. In addition to using the mutual-information objective function, PET/MRI fusion also included registration of whole mount pathology with established registration errors (10). Although we are aware that PET/MRI fusion imaging as performed in this study is limited because of unavoidable misregistration, this study may still prove valuable in assessing the clinical potential of future hybrid PET/MRI in prostate cancer.

MATERIALS AND METHODS

Patient Population

The study was conducted with 17 men (mean age ± SD, 60.5 ± 7.2 y) with biopsy-proven, untreated localized adenocarcinoma of the prostate scheduled to undergo prostatectomy; 14 patients had been included in our prior report on ^{11}C-choline (11). All patients received 12-sample prostate biopsies within 16 wk before enrollment, resulting in 3 or more cores positive for a summed Gleason score of 6 or greater from at least 1 lobe of the prostate. Patients with prior androgen ablation treatment, prostate biopsies performed less than 6 wk before PET/CT and MRI, previous external radiation treatment of the pelvic region, any prior malignancies, active inflammatory bowel disease, or evidence of prostatitis were not eligible.

In Vivo Imaging

In vivo imaging was performed within 14 d before radical prostatectomy (mean, 7.2 d; range, 3–13 d). In 14 cases, MRI and ^{11}C-choline PET/CT were performed on the same day, whereas in the remaining 3 cases imaging was completed 1 d apart. Anatomic in vivo MRI was performed either on a 3-T system (Achieva; Philips Healthcare) using a torso–cardiac surface coil or on a 1.5-T system (Signa; GE Healthcare) using a pelvic surface coil combined with an endorectal coil. Parameters for the axial T2-weighted scans on the 3-T system were fast spin echo (echo train length, 15); repetition time/echo time, 2,800/80 ms; field of view (FOV), 280 × 280 mm; matrix, 388 × 307; and twenty-eight 3-mm slices. Parameters on the 1.5-T system for the axial T2-weighted scans were fast spin echo (echo train length, 16); repetition time/echo time, 3,050/120 ms; FOV, 140 × 140 mm; matrix, 256 × 194; and twenty-eight 3-mm slices.

Axial diffusion scans obtained on the 1.5-T system only were single-shot echo planar imaging; repetition time/echo time, 6,000/65 ms; FOV, 240 × 240 mm; 128 × 128 acquired matrix reconstructed to a 256 × 256 matrix; 4-mm slices through the prostate; and isotropic diffusion weighting at b-values 0 and 800 s/mm^2. ADC maps were calculated by the standard formula (22):

$$ADC = (1/\mathrm{b})\ln[So/Sb], \quad \text{Eq. 1}$$

where So and Sb are diffusion-weighted image intensities acquired at b = 0 and 800 s/mm^2, respectively.

PET/CT was performed on a Siemens Biograph classic scanner, which incorporates an ECAT HR+ PET camera (Siemens) with a 2-channel helical CT component (n = 12). In 5 cases, PET/CT was performed on a Biograph TrueV HiRez scanner with an extended FOV and a 6-channel helical CT component (Siemens Medical Solutions). The intrinsic axial resolutions were approximately 5.2 and 4.5 mm in full width at half maximum, respectively, for the Biograph classic scanner (23) and Biograph TrueV HiRez scanner (11). Five minutes after injection of 690 ± 26 MBq of ^{11}C-choline, a limited body scan of the lower abdomen and pelvis was obtained (7 min per bed position), with the first bed position at the level of the prostate. A total of 2 bed positions were included on the Biograph TrueV and 3 on the Biograph classic PET scanner. Images were reconstructed in a 128 × 128 × 210 matrix, resulting in a 5.2 × 5.2 × 2.4 mm voxel dimension. Image reconstruction methods were identical on both scanners. Applying iterative (ordered-subset expectation maximization) algorithms (Fourier rebinning, 4 iterations, 8 subsets) with a 7-mm gaussian filter using a low-dose CT scan without intravenous or oral contrast for attenuation correction resulted in a similar effective axial reconstructed resolution on both scanners (11).

Image Coregistration

As described earlier, a standard registration method based on a mutual-information cost function and thin-plate spline deformation was applied (10,24). Although registration of in vivo modalities (T2-weighted MRI, DWI, PET/CT) is generally achieved without difficulties, our approach separated the difficult direct registration of histology and in vivo imaging (PET/CT, MRI) into achievable subregistration tasks involving intermediate ex vivo modalities (block-face photography and specimen MRI). Histology sections were corrected for 2-dimensional microtome-induced deformations by registering each section with its respective block-face photograph acquired immediately before cutting. Volumetric stacks of histology sections were then registered onto high-resolution (and high-information-content) ex vivo specimen MRI volumes. The final registration of the ex vivo specimen MRI volume onto the in vivo MRI reference integrated multiple discrete 2-dimensional histology slice volumes into the 3-dimensional in vivo reference space (T2-weighted MRI), with errors in the range of 2.26–3.74 mm (10).

Histologic Assessment

Fresh prostate specimens were fixed overnight in 10% neutral formalin. After specimen MRI at 3 T (10), the prostate was sectioned using a whole-mount technique and stained (hematoxylin and eosin [HE]) (25,26). Tumor maps were generated for each whole-mount slice to determine individual tumor foci in multifocal prostate cancers as previously described (27). Each tumor focus was assigned a primary and secondary Gleason grade and staged according to the 1998 guidelines of the American Joint Committee on Cancer (28). Tumors were graded according to Gleason scores, with ≤3 + 3 as low-, 3 + 4 as intermediate-, and ≥ 4 + 3 as high-grade tumors. Tumor borders were highlighted by the pathologist on HE slides. Benign hyperplasia was inhomogeneously present in prostatic tissues, favoring the central gland.

Image Data Analysis

Volumes of interest (VOI) were defined on the basis of registered HE histology, contouring the borders of each tumor lesion individually according to the pathologist's indications. Once HE slices were registered with T2-weighted MRI volumes, the tumor volume (cm^3) was determined. Depending on the tumor size per lobe, generally 2 (in 3 cases, just 1) separate standardized VOIs (1.5 cm^3) were defined in benign tissue in the peripheral zone and central gland, avoiding proximity to cancerous lesions. Those VOIs were then overlaid with the registered image volume (^{11}C-choline or ADC); thus, the definition of tumor lesions and benign reference background was independent from particular imaging features identified visually on each modality. Standardized uptake value (SUV) and ADC values were obtained on a voxel-by-voxel basis from every VOI by calculating the mean ± SD of SUVs and ADCs.

For parametric fusion PET/MRI, coregistered ^{11}C-choline SUV and ADC voxels were used to create parametric voxel ratio data with a simple quotient of SUV over ADC values.

$$\mathrm{P}_{CHOL/ADC}=\frac{^{11}\mathrm{C}-choline SUV}{ADC+0.001}. \quad \text{Eq. 2}$$

A small value of 0.001 was added to the ADC value in the denominator of Equation 2, thus avoiding division by zero. Because the quotient of ^{11}C-choline over ADC ($P_{CHOL/ADC}$) was computed in the reference MRI space, voxel dimensions and image matrix were identical to the T2-weighted MRI.

Further analyses were performed after calculating the mean tumor–to–benign prostate background ratio (TBR) using contralateral histologically benign tissue (which included areas of benign hyperplasia) as a reference. To account for variations of signal intensities on ADC maps and ^{11}C-choline uptake pattern within the prostate gland, smaller peripheral zone tumors were normalized by nonmalignant contralateral peripheral zone tissue, whereas larger tumors involving significant portions of the prostate lobe were normalized by the mean of the benign peripheral and central gland (11). For each modality (PET [SUV], MRI [ADC], and parametric fusion PET/MRI [$P_{CHOL/ADC}$], the same coregistered VOI ratios (TBRs) were used.

Statistics

Analyses were conducted using the R statistical package (29). For all analyses, we used a linear mixed-effects (LME) model. A Box-Cox transformation (a log transformation was suggested) was performed on all outcomes (^{11}C-choline, ADC, and $P_{CHOL/ADC}$). To minimize the impact of partial-volume effects on the data analysis, we used the tumor volume as a weighting factor. Tumors with a measured tumor volume below 0.7 cm^3 were down-weighted, whereas tumors ≥ 0.7 cm^3 were assessed without weighting. The level of the threshold was set at 0.7 as a compromise between image resolution of PET and MRI data. The unit of correlation for the LME models was the patient because several VOIs were measured within each subject. Contrasts (differences in model parameter estimates

associated with covariates) were used within the LME models for assessment of statistical significance using log-transformed TBRs to first compare each imaging method at 3 histologic levels (Gleason ≥ 3 + 4 vs. Gleason ≤ 3 + 3 vs. benign) and then the 3 imaging methods (PET vs. ADC vs. $P_{CHOL/ADC}$) at a Gleason ≥ 3 + 4 level. Multiple comparisons were adjusted by Bonferroni method.

RESULTS

All patients were staged T2b to T3b at pathology. The mean weight of the prostate specimen was 47.6 ± 12.1 g. The mean prostate-specific antigen level before biopsy was 7.6 ± 3.8 ng/mL.

A total of 51 tumor nodules were identified at HE histology. In all but 1 patient, multifocal disease was present. Gleason scoring of the largest (primary) tumor lesion per patient varied among 3 + 4 ($n = 7$), 4 + 3 ($n = 8$), and 4 + 4 ($n = 2$). Of 34 multifocal (secondary) tumor lesions, 28 were classified as Gleason ≤ 3 + 3, 4 as Gleason 3 + 4, and 2 as 4 + 4 disease. Tumor volumes, as identified on registered histology on T2-weighted MRI, varied with Gleason score categories. Low-grade tumors were considerably smaller (mean volume, 0.44 cm^3; range, 0.03–1.53 cm^3; $n = 29$) than intermediate- and high-grade disease. The average volume of intermediate-grade lesions was 4.00 cm^3 (range, 0.22–25.74 cm^3; $n = 10$), whereas high-grade lesions had similar average volume (4.09 cm^3) and range (0.34–12.63 cm^3; $n = 12$). Thus, many tumor volumes, mainly low-grade tumors, were below the reconstructed resolution of ^{11}C-choline PET/CT and DWI. In the statistical analyses, we accounted for partial-volume effects using the tumor volume (≤0.7 cm^3) as weighting factor.

For ^{11}C-choline, the mean TBR was significantly increased in Gleason ≥ 3 + 4 disease, compared with controls ($P < 0.05$) and significantly higher than Gleason ≤ 3 + 3 disease ($P < 0.01$) (Fig. 1A). Figure 1B shows that the mean ADC TBR decreased in Gleason ≥ 3 + 4 disease, compared with controls ($P < 0.05$), and was significantly lower than Gleason ≤ 3 + 3 disease ($P < 0.05$). For parametric PET/MRI using $P_{CHOL/ADC}$, the mean TBR was significantly elevated in Gleason ≥ 3 + 4 disease, compared with controls ($P < 0.005$), and also significantly higher than Gleason ≤ 3 + 3 disease ($P < 0.001$) (Fig. 1C).

Figure 2 displays imaging results of all modalities in high-grade disease using an overlay of PET, DWI, histology, and PET/MRI fusion imaging ($P_{CHOL/ADC}$) with T2-weighted MRI. A larger Gleason 4 + 3 lesion (volume, 6.78 cm^3) was identified visually on the left on ADC and ^{11}C-choline images. ^{11}C-choline PET images represent SUVs, whereas DWI displays ADC values. Accordingly, the PET/MRI fusion images represent $P_{CHOL/ADC}$. In addition, 1 separate low-volume Gleason 3 + 3 satellite lesion (volume, 0.36 cm^3) found in the peripheral zone on the right side was missed on all imaging.

Lesion identification on ADC and ^{11}C-choline imaging is strongly influenced by the image contrast between lesion and surrounding (benign) tissues. We therefore assessed whether the lesion-to-background contrast of Gleason ≥ 3 + 4 cancers differed for the 3 imaging modalities (PET, ADC, and fusion PET/MRI) using the imaging method as contrast in the LME model. We identified that the absolute TBRs of Gleason ≥ 3 + 4 cancers increased

from ADC to ^{11}C-choline PET/CT and from ^{11}C-choline PET/CT to $P_{CHOL/ADC}$, with each step being statistically significant (ADC vs. ^{11}C-choline PET/CT, $P < 0.02$; ADC vs. $P_{CHOL/ADC}$, $P < 0.05$; and ^{11}C-choline PET/CT vs. $P_{CHOL/ADC}$, $P < 0.01$). The positive effect on lesion identification is demonstrated in Figure 2.

DISCUSSION

The clinical behavior of primary prostate cancer ranges from microscopic, well-differentiated tumors to aggressive cancer with a high likelihood of invasion and metastasis. Clinical management can be most diverse and may range from definitive treatment options over localized treatments to watchful waiting. In the developed world, prostate-specific antigen testing has resulted in a dramatic stage-migration toward detection of lower-grade disease. In this situation, a reliable noninvasive detection of significant disease (30) could reduce unnecessary morbidity and treatment costs in patients with clinically indolent disease, thereby addressing the pressing issue of overtreatment of prostate cancer (31).

Imaging competes with the diagnostic transrectal prostate biopsy procedure, often performed repeatedly. Although the value of Gleason scoring based on final pathology obtained from prostatectomy specimens is undisputed as a reliable predictor of outcome, the accuracy of biopsy-based diagnosis is severely hampered by considerable sampling errors, resulting in significant under- or overestimation of the true Gleason score with limited concordance rates between 43% and 67% in contemporary studies (32–34).

We have recently shown in a partially overlapping patient population ($n = 14$) that—when TBRs are applied—^{11}C-choline preferentially localizes to aggressive prostate cancer (11). Here, we demonstrate in 17 patients that similar results can be obtained from DWI using ADC maps. Our data and several other recent studies indicate that ADCs are decreasing with increasing prostate cancer aggressiveness (14–17,35,36). However, similar to our findings regarding ^{11}C-choline, a considerable overlap between low-, intermediate-, and high-grade disease limits classification of individual tumor nodules.

Fusion of separately acquired PET and MRI has rarely been attempted in humans (37,38). Such approaches are severely hampered by unavoidable registration errors and temporal changes of functional image signals. Here, intermodality fusion between DWI and PET was assisted by high-resolution ex vivo MRI of the prostate specimen, which also offered the integration of registered histologic information. We have previously shown that registration between MRI and histology is possible with small errors (10), but with significant uncertainty in regard to lesion boundaries when using automated thresholding techniques (39). Fusion of in vivo imaging (MRI vs. PET/CT) is generally possible with sufficient precision; however, definitive measurements for the registration accuracy between in vivo PET/CT and MRI are lacking. In this study, in vivo PET/CT and MRI was performed mostly on the same day within a narrow time window, without endorectal coil and with voided urinary bladder. These precautions limited the potential for significant deformation of the prostate gland between scans.

Because Gleason ≥ 3 + 4 tumors, compared with low-grade cancers and benign prostate tissues, demonstrated significantly increased ^{11}C-choline uptake and decreased ADCs, we evaluated the potential value of fusion PET/MRI for lesion detection and characterization. Our results suggest that parametric PET/MRI using $P_{CHOL/ADC}$ significantly increased the lesion-to-benign background contrast (expressed by TBRs) for Gleason ≥ 3 + 4 tumors, compared with those obtained from ^{11}C-choline or ADC as a single modality. Despite improvements in characterization of Gleason ≥ 3 + 4 tumors, TBRs obtained from $P_{CHOL/ADC}$ in Gleason ≥ 3 + 4 still showed considerable overlap with low-grade disease and benign tissues, although to a lesser degree than TBRs from ^{11}C-choline and ADC (Fig. 1). We attribute such overlap—at least in part—to an increased variability of fusion data, compared with single-modality data, which is related to unavoidable registration errors. In the case of small lesions, even relatively minute registration errors may influence parameter estimates from PET/MRI fusion imaging. We accounted for this uncertainty by down-weighting low-volume disease for the statistical analyses.

Performing registration of histology with in vivo imaging has profound effects on the visual appearance of image data. It limits the FOV to the smallest component of the registration process (histology); thus, in vivo imaging registered to the reference space (T2-weighted MRI) can be visualized only for a confined anatomic space around the prostate gland as seen in Figure 2. Reformatting (warping) lower-resolution DWI and PET volumes to match the higher resolution of the reference space reduces voxel sizes for DWI and PET while maintaining their respective numeric data content (10), but reformatted DWI and PET images display an inferior visual clarity. Reformatting histology forces many high-resolution voxels to be replaced with 1 low-resolution voxel bearing the average intensity. As a result, the reformatted histology, compared with original HE slices, is blurred but sufficient to identify the exact lesion borders for VOI definition based on the pathologist's indications.

CONCLUSION

These pilot data are the first, to our knowledge, to suggest that parametric PET/MRI is feasible in humans and may improve identification of significant primary prostate cancer, a relevant question in the clinical management of primary disease. Obviously, parametric PET/MRI is not limited to the particular parameter ($P_{CHOL/ADC}$) presented here. Various other metabolic markers could be combined using diffusion- or perfusion-weighted MRI or MR spectroscopy to improve lesion detection or to enhance characterization for PET markers generally resulting in low contrast (such as hypoxia markers). Therefore, we anticipate parametric hybrid PET/MRI to be a versatile and potentially powerful imaging tool for prostate cancer and beyond.

Acknowledgments

We thank the staff of the PET and MRI suites for their excellent technical support. This research was supported by grants 1P01CA87634 and P50CA069568 (Prostate Cancer SPORE) and 1P01CA87634 (National Institutes of Health). No other potential conflict of interest relevant to this article was reported.

References

1. Scher B, Seitz M, Albinger W, et al. Value of ^{11}C-choline PET and PET/CT in patients with suspected prostate cancer. Eur J Nucl Med Mol Imaging. 2007; 34:45–53. [PubMed: 16932935]
2. Picchio M, Crivellaro C, Giovacchini G, Gianolli L, Messa C. PET-CT for treatment planning in prostate cancer. Q J Nucl Med Mol Imaging. 2009; 53:245–268. [PubMed: 19293771]
3. Picchio M, Briganti A, Fanti S, et al. The role of choline positron emission tomography/computed tomography in the management of patients with prostate-specific antigen progression after radical treatment of prostate cancer. Eur Urol. 2011; 59:51–60. [PubMed: 20869161]
4. Castellucci P, Fuccio C, Rubello D, et al. Is there a role for ^{11}C-choline PET/CT in the early detection of metastatic disease in surgically treated prostate cancer patients with a mild PSA increase <1.5 ng/ml? Eur J Nucl Med Mol Imaging. 2011; 38:55–63. [PubMed: 20848281]
5. Hara T, Kosaka N, Kishi H. PET imaging of prostate cancer using carbon-11-choline. J Nucl Med. 1998; 39:990–995. [PubMed: 9627331]
6. Kotzerke J, Prang J, Neumaier B, et al. Experience with carbon-11 choline positron emission tomography in prostate carcinoma. Eur J Nucl Med. 2000; 27:1415–1419. [PubMed: 11007527]
7. de Jong IJ, Pruim J, Elsinga PH, Vaalburg W, Mensink HJ. Visualization of prostate cancer with ^{11}C-choline positron emission tomography. Eur Urol. 2002; 42:18–23. [PubMed: 12121724]
8. Sutinen E, Nurmi M, Roivainen A, et al. Kinetics of [^{11}C]choline uptake in prostate cancer: a PET study. Eur J Nucl Med Mol Imaging. 2004; 31:317–324. [PubMed: 14628097]
9. Farsad M, Schiavina R, Castellucci P, et al. Detection and localization of prostate cancer: correlation of ^{11}C-choline PET/CT with histopathologic step-section analysis. J Nucl Med. 2005; 46:1642–1649. [PubMed: 16204714]
10. Park H, Piert MR, Khan A, et al. Registration methodology for histological sections and in vivo imaging of human prostate. Acad Radiol. 2008; 15:1027–1039. [PubMed: 18620123]
11. Piert M, Park H, Khan A, et al. Detection of aggressive primary prostate cancer with ^{11}C-choline PET/CT using multimodality fusion techniques. J Nucl Med. 2009; 50:1585–1593. [PubMed: 19759109]
12. Chenevert TL, Sundgren PC, Ross BD. Diffusion imaging: insight to cell status and cytoarchitecture. Neuroimaging Clin N Am. 2006; 16:619–632. [PubMed: 17148023]
13. Song I, Kim CK, Park BK, Park W. Assessment of response to radiotherapy for prostate cancer: value of diffusion-weighted MRI at 3 T. AJR. 2010; 194:W477–W482. [PubMed: 20489065]
14. Woodfield CA, Tung GA, Grand DJ, Pezzullo JA, Machan JT, Renzulli JF II. Diffusion-weighted MRI of peripheral zone prostate cancer: comparison of tumor apparent diffusion coefficient with Gleason score and percentage of tumor on core biopsy. AJR. 2010; 194:W316–W322. [PubMed: 20308476]
15. Turkbey B, Albert PS, Kurdziel K, Choyke PL. Imaging localized prostate cancer: current approaches and new developments. AJR. 2009; 192:1471–1480. [PubMed: 19457807]
16. Yoshimitsu K, Kiyoshima K, Irie H, et al. Usefulness of apparent diffusion co-efficient map in diagnosing prostate carcinoma: correlation with stepwise histopathology. J Magn Reson Imaging. 2008; 27:132–139. [PubMed: 18050334]
17. Kim CK, Park BK, Han JJ, Kang TW, Lee HM. Diffusion-weighted imaging of the prostate at 3 T for differentiation of malignant and benign tissue in transition and peripheral zones: preliminary results. J Comput Assist Tomogr. 2007; 31:449–454. [PubMed: 17538295]
18. Turkbey B, Shah VP, Pang Y, et al. Is apparent diffusion coefficient associated with clinical risk scores for prostate cancers that are visible on 3-T MR images? Radiology. 2011; 258:488–495. [PubMed: 21177390]
19. Pichler BJ, Judenhofer MS, Pfannenberg C. Multimodal imaging approaches: PET/CT and PET/MRI. Handb Exp Pharmacol. 2008:109–132. [PubMed: 18626801]
20. Boss A, Bisdas S, Kolb A, et al. Hybrid PET/MRI of intracranial masses: initial experiences and comparison to PET/CT. J Nucl Med. 2010; 51:1198–1205. [PubMed: 20660388]
21. Antoch G, Bockisch A. Combined PET/MRI: a new dimension in whole-body oncology imaging? Eur J Nucl Med Mol Imaging. 2009; 36(suppl 1):S113–S120. [PubMed: 19104802]

22. Chenevert, TL., Welsh, RC. Diffusion tensor MR imaging. In: Haacke, EM., editor. Current Protocols in Magnetic Resonance Imaging. Wiley Online Library; 2004. Available at: http://onlinelibrary.wiley.com/book/10.1002/0471142719. Accessed March 6, 2012
23. Herzog H, Tellmann L, Hocke C, Pietrzyk U, Casey M, Kuwert T. NEMA NU2-2001 guided performance evaluation of four Siemens ECAT PET-scanners. IEEE Nucl Sci Symp Conf Rec. 2003; 4:2836–2838.
24. Meyer CR, Boes JL, Kim B, et al. Demonstration of accuracy and clinical versatility of mutual information for automatic multimodality image fusion using affine and thin-plate spline warped geometric deformations. Med Image Anal. 1997; 1:195–206. [PubMed: 9873906]
25. Shah R, Bassily N, Wei J, et al. Benign prostatic glands at surgical margins of radical prostatectomy specimens: frequency and associated risk factors. Urology. 2000; 56:721–725. [PubMed: 11068287]
26. Shah R, Mucci NR, Amin A, Macoska JA, Rubin MA. Postatrophic hyperplasia of the prostate gland: neoplastic precursor or innocent bystander? Am J Pathol. 2001; 158:1767–1773. [PubMed: 11337374]
27. Mehra R, Han B, Tomlins SA, et al. Heterogeneity of TMPRSS2 gene rearrangements in multifocal prostate adenocarcinoma: molecular evidence for an independent group of diseases. Cancer Res. 2007; 67:7991–7995. [PubMed: 17804708]
28. Fleming, ID., Cooper, JS., Henson, DE. AJCC Cancer Staging Manual. 5th. Philadelphia, PA: Lippincott-Raven; 1997.
29. Ihaka R, Gentleman RR. A language for data analysis and graphics. J Comput Graph Statist. 1996; 5:299–314.
30. Krakowsky Y, Loblaw A, Klotz L. Prostate cancer death of men treated with initial active surveillance: clinical and biochemical characteristics. J Urol. 2010; 184:131–135. [PubMed: 20478589]
31. Bill-Axelson A, Holmberg L, Filen F, et al. Radical prostatectomy versus watchful waiting in localized prostate cancer: the Scandinavian prostate cancer group-4 randomized trial. J Natl Cancer Inst. 2008; 100:1144–1154. [PubMed: 18695132]
32. Cohen MS, Hanley RS, Kurteva T, et al. Comparing the Gleason prostate biopsy and Gleason prostatectomy grading system: the Lahey Clinic Medical Center experience and an international meta-analysis. Eur Urol. 2008; 54:371–381. [PubMed: 18395322]
33. Cookson MS, Fleshner NE, Soloway SM, Fair WR. Correlation between Gleason score of needle biopsy and radical prostatectomy specimen: accuracy and clinical implications. J Urol. 1997; 157:559–562. [PubMed: 8996356]
34. Fleshner NE, Cookson MS, Soloway SM, Fair WR. Repeat transrectal ultrasound-guided prostate biopsy: a strategy to improve the reliability of needle biopsy grading in patients with well-differentiated prostate cancer. Urology. 1998; 52:659–662. [PubMed: 9763089]
35. Katahira K, Takahara T, Kwee TC, et al. Ultra-high-b-value diffusion-weighted MR imaging for the detection of prostate cancer: evaluation in 201 cases with histopathological correlation. Eur Radiol. 2011; 21:188–196. [PubMed: 20640899]
36. Vargas HA, Akin O, Franiel T, et al. Diffusion-weighted endorectal MR imaging at 3 T for prostate cancer: tumor detection and assessment of aggressiveness. Radiology. 2011; 259:775–784. [PubMed: 21436085]
37. Ruf J, Lopez Hanninen E, Bohmig M, et al. Impact of FDG-PET/MRI image fusion on the detection of pancreatic cancer. Pancreatology. 2006; 6:512–519. [PubMed: 17106215]
38. Beer AJ, Eiber M, Souvatzoglou M, et al. Restricted water diffusibility as measured by diffusion-weighted MR imaging and choline uptake in ^{11}C-choline PET/CT are correlated in pelvic lymph nodes in patients with prostate cancer. Mol Imaging Biol. 2011; 13:352–361. [PubMed: 20490932]
39. Park H, Meyer CR, Wood D, et al. Validation of automatic target volume definition as demonstrated for 11C-choline PET/CT of human prostate cancer using multi-modality fusion techniques. Acad Radiol. 2010; 17:614–623. [PubMed: 20188602]

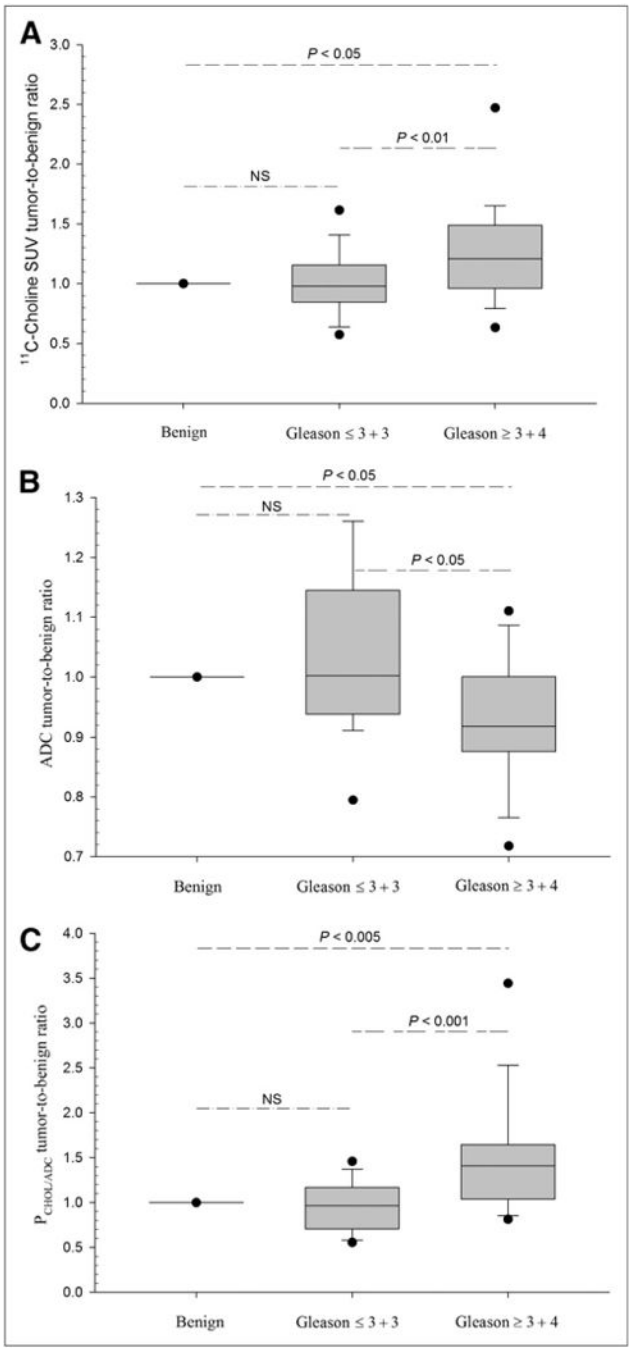

FIGURE 1.

Imaging results at Gleason score levels. Box-and-whisker plots showing imaging results in primary prostate cancer (for 2 Gleason score levels) with fifth and 95th percentile and outliers (●) are given for ^{11}C-choline SUV (A), ADC (B), and parametric fusion PET/MRI ($P_{CHOL/ADC}$) after normalization by benign control tissue (set to 1). Lesions with Gleason score ≥ 3 + 4 are significantly different from benign control tissue (long dashed lines) and Gleason score ≤ 3 + 3 lesions (short-long dashed lines), whereas Gleason score ≤ 3 + 3

lesions are not significantly different from controls (dashed-dotted lines) for all modalities (LME model).

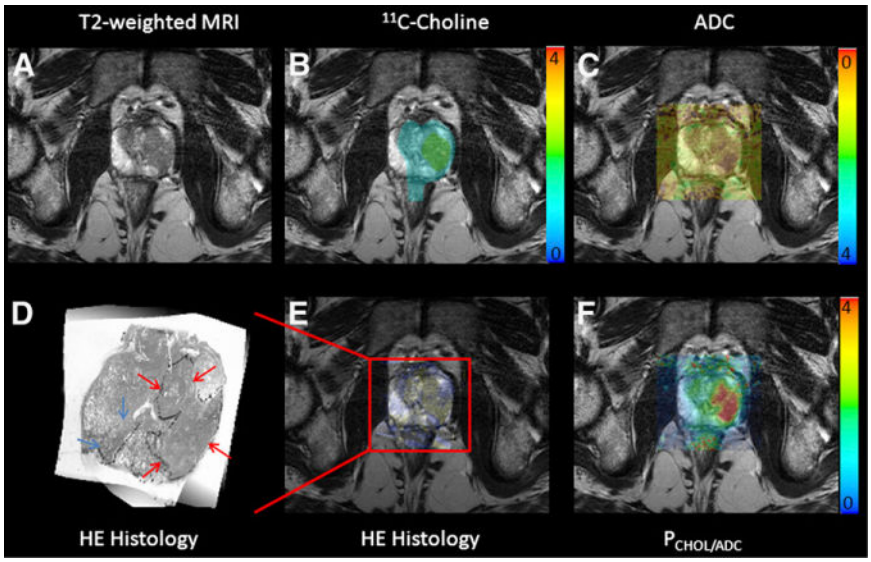

FIGURE 2.

Results of PET/MRI fusion imaging in high-grade prostate cancer. Specific image information derived from ^{11}C-choline PET (B), ADC DWI (C), HE histology (E), and parametric fusion PET/MRI using $P_{CHOL/ADC}$ (F) is coregistered with transaxial T2-weighted MRI (A). Color bars indicate ^{11}C-choline SUV (B), $P_{CHOL/ADC}$ (F), and inverted ADC (C). Zoomed registered HE histology slice is shown for increased clarity (D). At histology, Gleason 4 + 3 lesion is located in left lobe of prostate (red arrows) in peripheral and central zone, which is identified on registered imaging, whereas additional low-volume Gleason 3 + 3 lesion in right lobe is not identified (blue arrows).